OPTICA

Experimental post-selection loophole-free time-bin and energy-time nonlocality with integrated photonics

Francesco B. L. Santagiustina,[1,2] Costantino Agnesi,[2] Alvaro Alarcón,[3] Adán Cabello,[4,5] Guilherme B. Xavier,[3] Paolo Villoresi,[1,2] and Giuseppe Vallone[1,2,6,*]

[1]Istituto Nazionale di Fisica Nucleare (INFN)–Sezione di Padova, Via Marzolo 8, 35131 Padova, Italy
[2]Dipartimento di Ingegneria dell'Informazione, Università degli Studi di Padova, via Gradenigo 6B, 35131 Padova, Italy
[3]Institutionen för Systemteknik, Linköpings Universitet, SE-58183 Linköping, Sweden
[4]Departamento de Física Aplicada II, Universidad de Sevilla, E-41012 Sevilla, Spain
[5]Instituto Carlos I de Física Teórica y Computacional, Universidad de Sevilla, E-41012 Sevilla, Spain
[6]Dipartimento di Fisica e Astronomia, Università degli Studi di Padova, via Marzolo 8, IT-35131 Padova, Italy
*giuseppe.vallone@pd.infn.it

Received 30 June 2023; revised 16 January 2024; accepted 4 February 2024; published 12 April 2024

Time-bin (TB) and energy-time (ET) entanglements are crucial resources for long-distance quantum information processing. However, their standard implementations suffer from the so-called post-selection loophole that allows for classical simulation and thus prevents quantum advantage. The post-selection loophole has been addressed in proof-of-principle experiments. An open problem though is to close it in real-life applications based on integrated technologies. This is especially important since, so far, all integrated sources of TB and ET entanglements suffer from the post-selection loophole. Here, we report post-selection loophole-free certification of TB or ET entanglement in integrated technologies, by implementing in a silicon nitride chip the "hug" scheme [Phys. Rev. Lett. 102, 040401 (2009)] and certifying genuine TB entanglement through the violation of a Bell inequality.

https://doi.org/10.1364/OPTICA.499247

1. INTRODUCTION

Entanglement is a crucial resource in quantum communication protocols [1], including quantum key distribution [2], quantum teleportation [3], and quantum secret sharing [4]. Entanglement has also caused major debates [5,6], mainly concerning whether quantum systems have a hidden set of predetermined instructions (the so-called hidden variables) before a measurement operation is performed. This was settled by Bell, who showed that the assumptions of realism and locality cannot be simultaneously satisfied when the results from a correlation test are above a certain threshold [7]. The most widely used of these correlation tests is the Clauser-Horne-Shimony-Holt (CHSH) inequality [8], designed for bipartite systems with dichotomic measurement outputs. Due to experimental imperfections, a number of local hidden-variable models (LHVMs) have been derived over the years, which forces one to make assumptions in order to guarantee the validity of the Bell test [9]. Recently major advances were made in closing all major loopholes simultaneously in experiments [10–15], generating the possibility of ultra-secure device-independent quantum communication [16–18] and quantum random number generation [19–21]. Energy-time (ET) entanglement is a robust form of photonic entanglement that arises from the energy-time relation when photon pairs are produced in a non-linear medium [22]. First proposed by Franson [23], Bell tests on ET photon pairs have been widely used in many quantum communication schemes due to their robustness for long-distance propagation [22]. Time-bin (TB) entanglement, a popular modification where the excitation pump laser is already prepared in a superposition of an early and a late time-bin creating photon pairs in well-defined times, was demonstrated in 1999 [24]. A major issue with both these schemes is related to the discovery of local hidden-variable models (LHVMs), which explain the violation due to the post-selection of detection events, thus requiring extra assumptions to trust the Bell test result [25,26].

This post-selection loophole was first removed using hyper-entangled states [27], then exploiting a topologically different interferometric arrangement called the "hug" interferometer allowing genuine ET entanglement [28–32], and finally through the use of active optical switches for genuine TB entanglement production [33]. Removing the post-selection loophole is highly relevant since it has been exploited to experimentally hack ET and TB entanglement-based quantum key distribution systems [34]. Improved compatibility and stability requirements for TB and ET entanglement sources [35–37] have encouraged the use of novel

techniques such as quantum dots [38–41], micro-ring resonators on integrated photonics [42–51], and integrated waveguides [52–60]. However, the violation of Bell's inequality in these works cannot be fully certified due to the post-selection loophole present from the use of Franson's scheme.

In this work, we design an integrated photonics chip for the certification of both TB and ET entanglement sources, which is not affected by the post-selection loophole. Such versatility is obtained by extending the use of the hug scheme from the generation of genuine ET entanglement to genuine TB entanglement by introducing and demonstrating a rigorous post-selection procedure that closes the loophole. Our chip is based on a silicon nitride platform [61] and was designed to be inserted between a user's source and detectors. It contains the complete hug scheme including the required unbalanced Mach-Zehnder interferometers with thermal elements to apply the measurement operators for the Bell test. Our results show that the hug interferometer can be used to certify both genuine ET and TB entanglement sources, providing through a single photonic integrated chip (PIC) a solid verification tool that any user could use. This becomes particularly useful when dealing with uncharacterized or untrusted sources, a widely relevant topic in quantum communication networks.

2. GENUINE TIME-BIN ENTANGLEMENT GENERATION WITH THE HUG CONFIGURATION

A. Scheme and Model

This paper presents, to our knowledge, the first use of the hug configuration with a TB entangled state instead of an ET source pumped in continuous wave (CW) mode. Extending the use of the hug interferometer to the TB case allows a reduction in the frequency stability requirements of the pump laser and benefits from having specific photon generation times instead of a uniform distribution. This allows for synchronization of operations to be carried on the biphotons and eases the interference with other photons in more complex protocols. First, we will describe what state is obtained by feeding a time-bin entangled pair into an interferometer in the hug configuration and what is the resulting joint distribution of detection times of photons at the two analysis stations (that we will colloquially call Alice and Bob). Then we will tackle the issue of the post-selection loophole itself by describing a post-selection procedure adapted to the time-bin case that is completely local and does not open any loophole in the Bell test.

Consider the hug interferometer, consisting of two nested unbalanced interferometers composed of the two short arms A_S and B_S and the two long arms A_L and B_L, represented in Fig. 1 and the labeled input modes (C, D) and output modes of Alice (A_{+1}, A_{-1}) and Bob (B_{+1}, B_{-1}). We can define the corresponding creation operators at time-bin n as: $c_n^\dagger$, $d_n^\dagger$, $a_{+,n}^\dagger$, $a_{-,n}^\dagger$, $b_{+,n}^\dagger$, and $b_{-,n}^\dagger$. After the full measurement interferometers, the transformation is

$$c_n^\dagger \rightarrow \frac{1}{2}\left[e^{i\phi_{A_L}}\left(ia_{-,n+1}^\dagger - a_{+,n+1}^\dagger\right) + e^{i\phi_{B_S}}\left(b_{+,n}^\dagger + ib_{-,n}^\dagger\right)\right], \tag{1}$$

$$d_n^\dagger \rightarrow \frac{1}{2}\left[e^{i\phi_{B_L}}\left(ib_{-,n+1}^\dagger - b_{+,n+1}^\dagger\right) + e^{i\phi_{A_S}}\left(a_{+,n}^\dagger + ia_{-,n}^\dagger\right)\right]. \tag{2}$$

The input state consists of a pair of maximally entangled time-bin qubits. It can be produced by a source composed of a pulsed pump laser, an unbalanced interferometer, and a nonlinear device that generates photon pairs. We consider the interferometer imbalance to be inferior to half the pump repetition rate so that wavepackets generated by successive pulses will not interfere. The input state can be expressed as

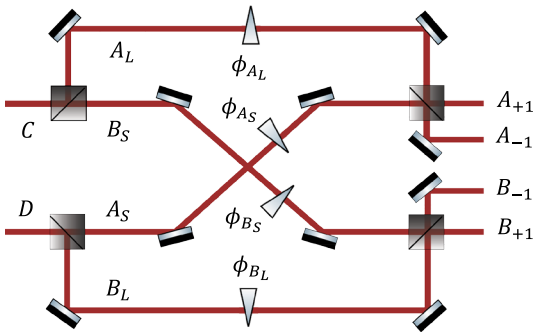

Fig. 1. Optical scheme representing with equivalent bulk components (balanced beam-splitters, mirrors, and glass wedges) the interferometer in the hug configuration integrated into the PIC. Labels indicate the different spatial modes and phase-shifts ($\phi_{A_L}, \phi_{A_S}, \phi_{B_S}, \phi_{B_L}$).

$$|\Phi_{\text{in}}\rangle \triangleq \frac{1}{\sqrt{2}}\left(c_1^\dagger d_1^\dagger + e^{i\phi_p} c_2^\dagger d_2^\dagger\right)|0\rangle \triangleq \frac{1}{\sqrt{2}}\left(|ee\rangle + e^{i\phi_p}|ll\rangle\right), \tag{3}$$

where ϕ_p is a phase associated to the pump interferometer. This state is transformed by the measurement interferometers into

$$\begin{aligned}
&\frac{1}{4\sqrt{2}}\left[e^{i\phi_{A_L}}\left(ia_{-,2}^\dagger - a_{+,2}^\dagger\right) + e^{i\phi_{B_S}}\left(b_{+,1}^\dagger + ib_{-,1}^\dagger\right)\right] \\
&\quad\times\left[e^{i\phi_{B_L}}\left(ib_{-,2}^\dagger - b_{+,2}^\dagger\right) + e^{i\phi_{A_S}}\left(a_{+,1}^\dagger + ia_{-,1}^\dagger\right)\right]|0\rangle \\
&\quad+\frac{e^{i\phi_p}}{4\sqrt{2}}\left[e^{\phi_{A_L}}\left(ia_{-,3}^\dagger - a_{+,3}^\dagger\right) + e^{\phi_{B_S}}\left(b_{+,2}^\dagger + ib_{-,2}^\dagger\right)\right] \\
&\quad\times\left[e^{i\phi_{B_L}}\left(ib_{-,3}^\dagger - b_{+,3}^\dagger\right) + e^{i\phi_{A_S}}\left(a_{+,2}^\dagger + ia_{-,2}^\dagger\right)\right]|0\rangle.
\end{aligned} \tag{4}$$

From the above equation, we can note that two photons can be detected in different time-bins if and only if they are both detected on the same measurement station, either at Alice or at Bob. This will happen with probability $\frac{1}{2}$. Let us now focus on the subspace where one photon arrives at Alice and one at Bob, in any time-bin:

$$\begin{aligned}
&\frac{e^{i\left(\phi_{A_L}+\phi_{B_L}\right)}}{4\sqrt{2}}\left[e^{i(2\Delta\phi-\phi_p)}\left(b_{+,1}^\dagger + ib_{-,1}^\dagger\right)\left(a_{+,1}^\dagger + ia_{-,1}^\dagger\right)\right. \\
&\quad\left.+\,e^{i\phi_p}\left(ia_{-,3}^\dagger - a_{+,3}^\dagger\right)\left(ib_{-,3}^\dagger - b_{+,3}^\dagger\right)\right]|0\rangle \\
&\quad+\frac{e^{i\left(\phi_{A_L}+\phi_{B_L}+\Delta\phi\right)}}{2\sqrt{2}}\left[\cos(\Delta\phi)\left(a_{+,2}^\dagger b_{+,2}^\dagger - a_{-,2}^\dagger b_{-,2}^\dagger\right)\right. \\
&\quad\left.-\,\sin(\Delta\phi)\left(a_{-,2}^\dagger b_{+,2}^\dagger + a_{+,2}^\dagger b_{-,2}^\dagger\right)\right]|0\rangle \\
&\quad\triangleq\frac{e^{i\left(\phi_{A_L}+\phi_{B_L}\right)}}{4\sqrt{2}}\left[e^{i(2\Delta\phi-\phi_p)}|\chi_{1,1}\rangle + e^{i\phi_p}|\chi_{3,3}\rangle\right] \\
&\quad+\frac{e^{i\left(\phi_{A_L}+\phi_{B_L}+\Delta\phi\right)}}{2\sqrt{2}}|\chi_{2,2}\rangle,
\end{aligned} \tag{5}$$

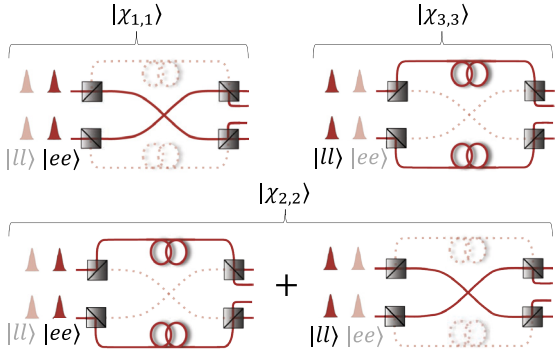

Fig. 2. Schemes representing the three processes leading to detections at both Alice and Bob. The state $|ee\rangle$ ($|ll\rangle$) corresponds to photon pairs generated by the early (late) pump pulse. Case $|\chi_{1,1}\rangle$ ($|\chi_{3,3}\rangle$) corresponds to pairs generated by the early (late) pump pulse taking the short (long) paths. Case $|\chi_{2,2}\rangle$ corresponds to the superposition where photons from the early pump pulse taking the long paths interfere with the photons from the late pump pulse taking the short paths.

where

$$\Delta\phi \triangleq \frac{1}{2}\left(\phi_p + \phi_{A_S} + \phi_{B_S} - \phi_{A_L} - \phi_{B_L}\right), \tag{6}$$

and the three kets, $|\chi_{1,1}\rangle$, $|\chi_{2,2}\rangle$, and $|\chi_{3,3}\rangle$, correspond to coincident detections at any of Alice and Bob detectors in the first, second, and third time-bins, respectively. We note that thanks to the hug configuration, whenever a photon is detected at Alice and the other at Bob, they are detected in the same time-bin. The processes leading to these three possible coincidence times are illustrated in Fig. 2. Coincidences in time-bins 1 and 3 do not display interference as they are due to a single process. Conditioned on detection at Alice and Bob, they happen with equal probabilities of $\frac{1}{4}$. Thus, detection on central time-bins happens with probability $\frac{1}{2}$, and results from the superposition of two processes, which leads to two-photon interference; the relevant term is indeed

$$|\chi_{2,2}\rangle = \Big[\cos(\Delta\phi)\left(a^\dagger_{+,2}b^\dagger_{+,2} - a^\dagger_{-,2}b^\dagger_{-,2}\right) - \sin(\Delta\phi)\left(a^\dagger_{-,2}b^\dagger_{+,2} + b^\dagger_{-,2}a^\dagger_{+,2}\right)\Big]|0\rangle, \tag{7}$$

which displays full interferometric visibility. Coincidences in the central time-bin are the ones displaying non-local correlations; the next section will explain how it is possible to post-select them without introducing a loophole in Bell tests.

B. Local Post-Selection Procedure for Genuine Time-Bin Entanglement

The post-selection loophole derives from the possibility that the set of events post-selected by the two partners depends on the measurement settings. In that case, the original Bell inequalities do not apply in general to the post-selected sets and must be suitably adapted. For some post-selection schemes, the local realistic bound becomes so high that it cannot be exceeded with quantum states.

In the hug configuration, the two measurement interferometers are connected such that detections at both Alice and Bob can only be due to the two down-converted photons propagating on paths of the same length: either both taking the short paths or both taking the long paths. In the ET case, it is thus sufficient to discard events where two photons are received on the same side leaving coincidence events that always result from the two-photon interference of these two indistinguishable processes [29]. In the TB case instead, a local post-selection based on the photon detection times will be necessary. The distribution of detection times and the post-selection windows are represented in Fig. 3 and compared to what one obtains using a Franson interferometer with the same input state. When looking at the histogram of the difference between detection times of Alice and Bob, plotted in Fig. 3(a), we have a single peak as the generation time and the traveled optical path lengths are equal. The photons will always be detected in coincidences; however, we have three possible detection times with respect to the pump pulse emission, as illustrated in Fig. 3(b). This leads to the same three-peak histogram of detection times that is obtained by using the Franson interferometer and only the photon pairs detected in the central TB display interference (case $|\chi_{2,2}\rangle$ in Fig. 2). Coincidences in the first and last TBs can instead be associated with a single known emission time and propagation path (cases $|\chi_{1,1}\rangle$ and $|\chi_{3,3}\rangle$ in Fig. 2). The fact that detections in the central time-bin for one partner always correspond to events displaying two-photon interference will allow them to perform a local post-selection of events that is independent of both local and remote measurement settings so that the original CHSH inequality can still be applied.

Alice and Bob can, independently, post-select the detections in the central time-bin and they will end up with the same set of events. In a Bell test scenario, the measurement settings are randomly switched fast enough to guarantee space-like separation of the measurement choices. In that way, the post-selection at Alice cannot depend on the measurement choice of Bob and vice-versa. The post-selection could still depend on the local measurement settings, but if it did one detection would be selected by Alice and independently discarded by Bob (or vice-versa) for some hidden variables, as the selections would depend on the local measurement setting choices, which are assumed to be independent random variables. Thus, obtaining an equal set of post-selected events without communication certifies that the set of post-selected coincidences is independent of the measurement settings. In that case, there is no change of ensemble for the estimation of the correlations in the various measurement settings and the original CHSH inequality can be applied [62].

In practice, it may happen that a detection happens on the central peak for one of the partners and on a lateral peak for the other. This can mainly be caused by double pairs, failed separation of the signal and idler photons, and, finally, detection temporal jitter. Considering this, the independence from local phase settings of the post-selection can no longer be guaranteed; however, the post-selection remains local. The post-selection of events is said to be local if it only depends on the state hidden variable and on the local measurement setting. In that case, the discarded events can be considered as missing detections and approaches developed to close the efficiency loophole can be applied. One of them, proposed in Ref. [63], consists of assigning a fixed outcome of zero to events undetected (in our case, locally discarded) by only one partner. With this approach, the original local-realist CHSH bound of two holds on the union of events where at least one partner detected (in our case, locally post-selected) a photon. These events will lower the violation but thanks to the geometry of the hug configuration they will remain very rare and mainly due to higher order emissions of the generation process.

The complete post-selection procedure to obtain a valid violation, as detailed in Appendix A, is thus the following.

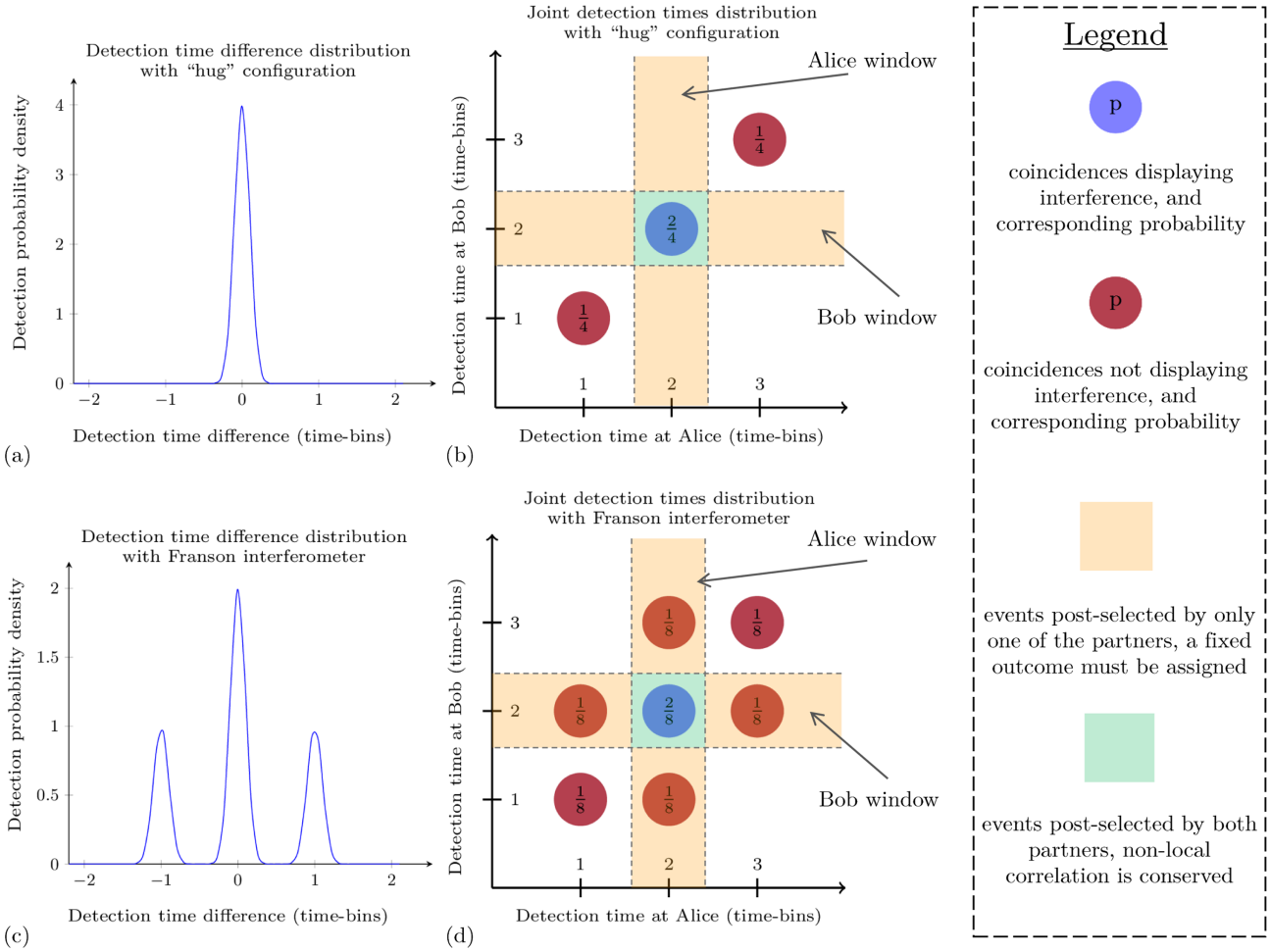

Fig. 3. Theoretical distributions of detection times for time-bin entanglement with different receivers. On the top, the hug configuration is considered and the distributions of the detection time difference (between Alice and Bob detectors) showing a single peak is plotted (a) along with a scheme showing the joint probability distribution of photon detection times (b). On the bottom, the Franson configuration is considered for which the detection time difference histogram displays three peaks (c) as we have additional combinations of possible detection times as shown in (d). Local post-selection windows are indicated on the joint distribution schemes as colored bands (see legend). With the hug configuration, one photon is only detected at both Alice and Bob detectors if the two photons have traveled the same length; thus the time correlation of the input state is conserved. The orange area ideally does not contain any counts as all detections happen in coincidence in the three possible time-bins [cases $|\chi_{1,1}\rangle$, $|\chi_{2,2}\rangle$, and $|\chi_{3,3}\rangle$ of Eq. (5)]. Hence Alice and Bob by locally post-selecting detections on time-bin 2 will select the same set of events, which are displaying full interferometric visibility and can result in a CHSH parameter up to $2\sqrt{2}$. This is not possible for the Franson interferometer as a detection in time-bin 2 at one partner can correspond to a detection in any of the three time-bins at the other, which results in a maximal attainable CHSH parameter of $\frac{2\sqrt{2}}{3} \approx 0.94 < 2$.

1. Alice and Bob tell each other for which pump pulses they detected a photon in any of their detectors and in any time-bin. If the losses do not allow a detection-loophole-free experiment, we can only proceed under the fair sampling hypothesis [8] and consider the subset of events where both photons were detected as representative of the totality of events.
2. The 50% of events where both photons are detected by the same partner are rightfully discarded as the selected events are independent of remote and local phase settings (this can be verified by switching randomly the phase settings at a high enough rate) [29].
3. Alice and Bob locally post-select the detections forming the central peak of their detection time histogram by defining an appropriate window. They communicate to each other which events they have selected. If only one of the partners selected an event, the other one considers the twin photon as lost (even if actually it was received but not in the central peak) and assigns a fixed value of zero to the outcome of the measure for that run, as it is done to deal with the efficiency loophole [9,63].

The same local post-selection would not allow a violation if the measurement was performed with a Franson interferometer. Franson's scheme consists of injecting each photon in separated but identical unbalanced interferometers whose delays are greater than the single photon coherence time. In the TB case, the pump interferometer must have the same imbalance as the measurement interferometers. We consider the case where the interferometers are composed of passive beam-splitters (also called "phase-time encoding" [64]) and do not feature switches that would allow the generation of genuine time-bin entanglement without any post-selection as in Ref. [33]. In this case, the perfect correlation of detection times is lost as the path choices (and resulting delays) at Alice's and Bob's measurement interferometers are independent,

which results in a histogram of the difference between detection times of Alice and Bob with three peaks, as plotted in Fig. 3(c). We have again three possible detection times for each photon, but as shown in Fig. 3(d), the joint distribution of detection times is different from that obtained with the hug. Only events detected in the central time-bin by both partners maintain a path superposition and display interference. This set corresponds to only $\frac{1}{4}$ of all detections. Other detections lead indeed to uncorrelated outcomes so no violation of Bell inequalities can actually be obtained with Franson's interferometer when considering all events and a local post-selection of detections in time-bin 2 will result in only $\frac{1}{3}$ of the events selected by both partners, which brings the maximum value of the Bell parameter to $\frac{2\sqrt{2}}{3} < 2$ as fixed outcomes resulting in null correlations must be assigned to the remaining $\frac{2}{3}$ of events. With the hug configuration instead, when a photon is detected in the central time-bin by one partner it is generally also detected in the central time-bin by the second partner. Only non-idealities in the input state or in the experimental setup lead to events post-selected solely at one side, so if the two-photon interference visibility is sufficient we will still be able to obtain a violation of the CHSH inequality.

3. EXPERIMENTAL REALIZATION

A. Experimental Setup and Integration of the Hug Interferometer on Silicon Nitride

The experimental setup is shown in Fig. 4. A mode-locked Ti:sapphire laser is used to produce pump pulses of a few picoseconds at a rate of 76 MHz. The pulses are sent to a Michelson interferometer with an optical path-length imbalance between the two arms matching the imbalance between the short and long paths in the chip interferometers. Pulses are then coupled into a polarization-maintaining single-mode fiber and sent to a periodically poled potassium titanyl phosphate (ppKTP) waveguide. The wavelength of the pump laser is tuned to 775 nm so that the two photons produced through the degenerate spontaneous parametric down-conversion (SPDC) process have a spectrum centered around 1550 nm, which enables the use of C-band components and efficient propagation in optical-fiber-based telecommunication networks. The pump pulses are separated from the biphotons through a long-pass dichroic filter. Since type-II SPDC phase matching is used, the signal and idler can be separated by a polarization beam-splitter (PBS) and then sent to the two inputs of the PIC. The PIC inputs and outputs are each butt-coupled via a fiber array using fiber alignment stages with micrometric precision. In contrast to what happens with a Franson interferometer, when using the hug configuration (with symmetric delays) it is essential to match the time of arrival of the two photons' wavepackets at the input beam-splitters (BS) of the interferometer (see Appendix B). A free-space delay line, built using a micrometric stage, was needed before the PIC to compensate for this mismatch.

As anticipated, the hug interferometer (with its phase modulators) is integrated into the photonic chip based on the Triplex silicon nitride (Si_3N_4) platform manufactured by LioniX [61]. This platform employs an asymmetric double-stripe cross-section structure for the waveguides surrounded by silicon dioxide (SiO_2), which is optimal for propagation due to the low losses. The high contrast in the refractive index also allows for low bending losses, which is very relevant to implement delays necessary for the construction of the hug structure. The schematic of the chip is also shown in Fig. 4, where spot size converters are employed to couple the light from single-mode telecom fibers to match the mode of the double-stripe waveguides on the chip. Following the two input paths, two 50:50 bidirectional couplers, working as beam-splitters (BS), are employed to create four parallel paths. Two long delay lines, corresponding to 116 ps time delay, made from waveguide spirals are placed in two of the paths to create the long arms, which are then followed by two thermal phase shifters. These are controlled by the heat produced from an electrical current flowing through a thin gold wire deposited on top of the waveguide. The other two parallel arms (short), are crossed to create the hug configuration by connecting to the opposite party. Then, the two upper and lower paths are connected to two 50:50 bidirectional couplers where the final joint projection is made. The four outputs are then led out of the chip through the use of spot-size converters, where an array of single-mode fibers is aligned at the chip's edge and reaches superconducting nanowire single-photon detectors

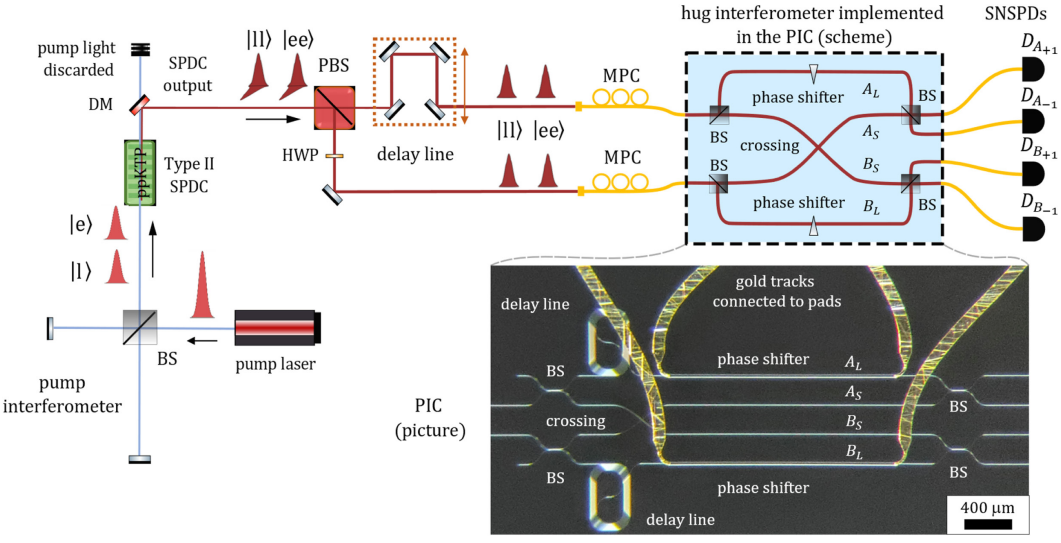

Fig. 4. Overview scheme of the experimental setup used to generate time-bin entangled states and certify their entanglement. BS: beam-splitter, D: detector, DM: dichroic mirror, HWP: half-wave plate, MPC: manual polarization controllers, PBS: polarizing beam-splitter, PIC: photonic integrated chip, SNSPDs: superconducting nanowire single-photon detectors, SPDC: spontaneous parametric down-conversion.

(SNSPDs) with on-average detection efficiency of 69%, RMS jitter of 8.3 ps, and dark-counts rate of 100 Hz. The overall insertion loss from the PIC is 8.8 dB, of which more than 6 dB is due to coupling. These losses are not compatible with an efficiency-loophole-free violation so we will assume the fair-sampling hypothesis [9] and consider runs where both photons were detected as representative.

Implementing the hug interferometer fully on a PIC allows for intrinsic phase stability and further shows the versatility of the hug interferometer as a characterization device by working for both TB, as shown here, and ET sources, as shown in previous works [30–32].

B. Results and Discussion

The input state was tested by attempting a violation of the CHSH inequality. The measurements in the two bases at Alice and Bob were performed by tuning the phase differences between the long and the short arms of the interferometers to the appropriate values. To calibrate the thermal phase-shifters, a scan over voltages of the post-selected coincidence rates was performed, leading through two-photon interference to the characteristic sinusoidal modulation of the coincidence counts as shown in Fig. 5.

To minimize the reduction of the Bell parameter due to the local post-selection procedure, it is essential to have a separation between the time-bins allowing for clear discrimination of the events belonging to the central peaks and to the lateral peaks. Assuming a Gaussian distribution of the detection time moduli for each time-bin, the delay of 116 ps between long and short arms in our PIC required us to lower the standard deviation of such Gaussians around 20 ps to have a negligible impact on the CHSH violation. The use of low-jitter SNSPD detectors (Single Quantum Eos) and time-taggers (Qutools QuTAG), along with a high precision synchronization to the fluctuations of the pump laser repetition rate allowed us to achieve this. First, we derived through frequency synthesis on an FPGA a signal at 10 MHz locked to the 76 MHz signal of the pump laser, which was used as clock for our time-tagger. Then, given that we could still observe a drift in the average detection time modulus for each time-bin, we implemented a real-time interpolation algorithm allowing us to correct for this drift and achieve arrival time distributions with standard deviations as low as 8.2 ± 0.1 ps as shown in Fig. 6 when detection rates are high enough to sample the drift (see Appendix C for further details).

The Bell test was performed by measuring the correlations in the four different basis combinations by maintaining the corresponding phase-shifters' voltages in a predetermined sequence. A value of $S_{\mathrm{LP}} = 2.42 \pm 0.05$ was obtained, which represents a violation of the CHSH inequality by more than seven standard deviations. We identified several factors lowering the value of the violation. First, the visibility of the two-photon interference in the hug configuration depends on the indistinguishability between the signal and idler photons, which we assessed through Hong-Ou-Mandel interference to be $94.7 \pm 0.3\%$ for this Type II SPDC source. Second, the output beam-splitters of our interferometer were not perfectly balanced. We measured power-splitting ratios of $55.6 \pm 0.1\%$ and $56.02 \pm 0.04\%$; similar fabrication imperfections of silicon nitride directional couplers were also mentioned in Ref. [59]. The interferometric visibility measured in the central peak by scanning the pump interferometer was $89.2 \pm 0.7\%$ for around 700 coincidences per second. The experiment also suffered from thermal cross-talk between the phase-modulators, introducing a phase drift, which reduced the violation and limited to a dozen seconds the measurement time in each setting. Longer acquisitions led to violations of more than 10 standard deviations at the price of a reduced Bell parameter. This problem, also reported in other works using the same platform [65,66], could be avoided by further distancing between the phase-shifters, the use of isolation trenches, or thermoelectric cooling [67]. Finally, the local post-selection procedure also reduces the Bell parameter by about 0.06 with respect to the non-local post-selection. Even if this might be considered a fair price for closing the post-selection loophole, we stress that this reduction is only due to the experimental parameters mentioned in Section 2.B, which lead to non-null lateral peaks in the arrival-time differences histogram shown in Fig. 7, but could be improved.

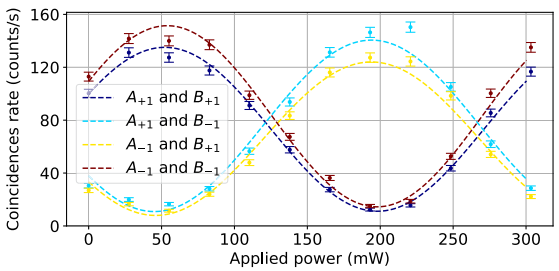

Fig. 5. Modulation by interference of the coincidence rates in the central peak (100 ps window) versus power applied to Alice's thermal phase-shifter. Measured data as dots with one standard deviation error bars and sinusoidal fit as dashed lines.

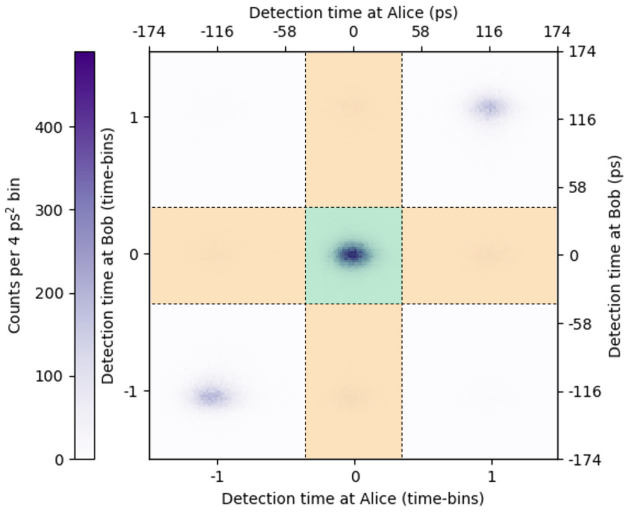

Fig. 6. Joint histogram of detection time moduli at Alice and Bob using the hug interferometer in our PIC, to be compared to the theoretical prediction of Fig. 3(b). Our clock drift correction algorithm allows us to obtain detection time distributions for each time-bin with standard deviations as low as 8.2 ± 0.1 ps, so that the three time-bins can be clearly discriminated despite the interferometer's imbalance of just 116 ps. The vertical and horizontal bands represent the post-selection windows of Alice and Bob. In our Bell tests, the union of the two sets is considered, and fixed outcomes are assigned to the few events discarded by only one partner (orange bands) so that the original CHSH bound of two is maintained for LHVMs.

4. CONCLUSIONS

As all past chip-based demonstrations of energy-time (ET) and time-bin (TB) entanglements exploited the Franson scheme, their

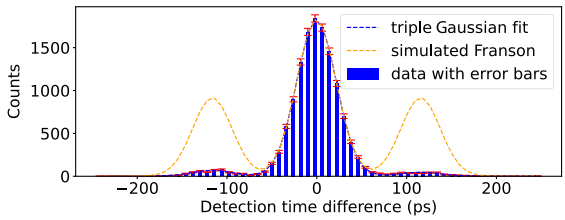

Fig. 7. Histogram of detection time differences for arrivals at detectors $D_{A_{+1}}$ and $D_{B_{+1}}$ with bin-width of 8 ps. Data measured during the Bell test with one standard deviation error bars and best fit using as model the mixture of three Gaussian distributions with means shifted by one time-bin each. Note how the lateral peaks are reduced with respect to the simulated Franson scheme. From the fit, the lateral peaks jointly account for about 5.7% of the events. The larger width of the Gaussian with respect to Fig. 6 is due to the lower biphoton generation rate used in the Bell test to reduce double pairs, which impacts the clock drift correction algorithm.

security was undermined by the post-selection loophole [26]. Here, we have shown how a different interferometric scheme, the hug configuration [29], can be used to close the post-selection loophole not only in ET entanglement [30–32], but also, as demonstrated in this paper, in TB entanglement. Implementing a hug interferometer inside a photonic integrated circuit (PIC) thus provides a post-selection loophole-free certification tool for both TB and ET entanglements. We used the PIC to test a time-bin entangled state, reporting a CHSH-Bell parameter of 2.42 ± 0.05, which represents a violation by more than seven standard deviations of the local realistic bound of two, which remains valid with our post-selection procedure. It is important to note that genuine (i.e., post-selection loophole-free) time-bin entanglement had been only been demonstrated in Ref. [33], which exploited high speed optical switches, whereas here we report, for the first time, genuine time-bin entanglement with a fully passive scheme. Demonstrating the use of a PIC to certify sources of genuine TB/ET entanglement is an important achievement in the field of quantum communication and a step forward toward a secure quantum communication platform. Future steps to improve the presented design could include mitigation of thermal cross-talk in the PIC and the use of tunable beam-splitters implemented through Mach-Zehnder interferometers [68] to increase the interferometric visibility. Further improvements would be necessary to close the remaining loopholes that affect our implementation. The losses due to the coupling between fibers and the PIC waveguides could be reduced with the use of state-of-the-art tapers, which could reduce losses to only 0.3 dB per facet [69,70]. Furthermore, if the entangled photon pair source and detectors are integrated into the same chip, the coupling losses are no longer relevant and we can benefit from the low propagation losses (0.1 db/cm) of silicon nitride so that the efficiency loophole could be closed. The locality loophole and the freedom-of-choice loopholes are particularly challenging to close on an integrated device including both receivers. However, one approach could be to use electro-optical phase modulators to alternate between measurement settings. Indeed, silicon modulators can reach bandwidths over 100 GHz [71], which would only require a separation of a few millimeters to ensure space-like separation. Silicon nitride modulators could also be sufficient as bandwidths of 15 GHz have been reported [72], which would correspond to a separation of a few centimeters, which remains feasible.

APPENDIX A: DETAILS ON THE POST-SELECTION PROCEDURE

1. CHSH Inequality for Outcomes of Absolute Value Bounded to 1

Hereafter, we reproduce for reference (with some editorial changes to make it self-contained) the CHSH inequality as stated on pp. 4-5 of Ref. [9].

The outcomes of the experiment are described by random variables [e.g., $A(\lambda)$] that are maps from the sample to the possible outcomes of the experiment, and the expected (average) outcome of an experiment can be calculated as

$$E(A) = \int_\Lambda A(\lambda) \mathrm{d}P(\lambda) = \int_\Lambda A(\lambda)\rho(\lambda)\mathrm{d}\lambda, \tag{A1}$$

the latter if ρ can be constructed. In this notation, the CHSH inequality can be written.

Theorem 2. (Clauser, Horne, Shimony, and Holt [8], Bell [73]) The following four prerequisites are assumed to hold except at a set of zero probability.

(i) Realism. Measurement outcomes can be described by two families of random variables (A for site 1 with local setting a, B for site 2 with local setting b):

$$A(a, b, \lambda) \quad \text{and} \quad B(a, b, \lambda).$$

The dependence on the hidden variable λ is usually suppressed in the notation.

(ii) Locality. Measurement outcomes are independent of the remote setting:

$$A(a, \lambda) \stackrel{\text{def}}{=} A(a, b_1, \lambda) = A(a, b_2, \lambda),$$

$$B(b, \lambda) \stackrel{\text{def}}{=} B(a_1, b, \lambda) = B(a_2, b, \lambda).$$

For brevity denote $A_i(\lambda) = A(a_i, \lambda)$ and $B_j(\lambda) = B(b_j, \lambda)$.

(iii) Outcome restriction. Measurement outcomes are bounded in absolute value by 1:

$$|A(a, \lambda)| \leqslant 1 \quad \text{and} \quad |B(b, \lambda)| \leqslant 1.$$

Then,

$$|E(A_1B_1) + E(A_1B_2)| + |E(A_2B_1) - E(A_2B_2)| \leqslant 2.$$

Proof:

$$\begin{aligned}
&|E(A_1B_1) - E(A_1B_2)| \\
&= \left|E\Big(A_1B_1 \pm A_1B_1A_2B_2 - (A_1B_2 \pm A_1B_1A_2B_2)\Big)\right| \\
&\leqslant E\Big(|A_1B_1(1 \pm A_2B_2)| + |A_1B_2(1 \pm A_2B_1)|\Big) \\
&\leqslant 2 \pm (E(A_2B_2) + E(A_2B_1)).
\end{aligned}$$

The proof is further detailed with a different but equivalent notation in the original article of Bell [73], which we reproduce (with some editorial changes to make it self-contained).

The correlation function is written as

$$P(\hat{a},\hat{b}) = \int \mathrm{d}\lambda \rho(\lambda) \bar{A}(\hat{a},\lambda)\bar{B}(\hat{b},\lambda),$$

so that

$$\begin{aligned} P(\hat{a},\hat{b}) - P(\hat{a},\hat{b}') &= \int \mathrm{d}\lambda \rho(\lambda) \left[\bar{A}(\hat{a},\lambda)\bar{B}(\hat{b},\lambda) - \bar{A}(\hat{a},\lambda)\bar{B}(\hat{b}',\lambda)\right] \\ &= \int \mathrm{d}\lambda \rho(\lambda) \Big[\bar{A}(\hat{a},\lambda)\bar{B}(\hat{b},\lambda) \pm \bar{A}(\hat{a},\lambda)\bar{B}(\hat{b},\lambda)\bar{A}(\hat{a}',\lambda)\bar{B}(\hat{b}',\lambda) \\ &\quad - \left(\bar{A}(\hat{a},\lambda)\bar{B}(\hat{b}',\lambda) \pm \bar{A}(\hat{a},\lambda)\bar{B}(\hat{b},\lambda)\bar{A}(\hat{a}',\lambda)\bar{B}(\hat{b}',\lambda)\right)\Big] \\ &= \int \mathrm{d}\lambda \rho(\lambda) \left[\bar{A}(\hat{a},\lambda)\bar{B}(\hat{b},\lambda)\left(1 \pm \bar{A}(\hat{a}',\lambda)\bar{B}(\hat{b}',\lambda)\right)\right] \\ &\quad - \int \mathrm{d}\lambda \rho(\lambda) \left[\bar{A}(\hat{a},\lambda)\bar{B}(\hat{b}',\lambda)\left(1 \pm \bar{A}(\hat{a}',\lambda)\bar{B}(\hat{b},\lambda)\right)\right], \end{aligned}$$

and by applying the conditions $|\bar{A}| \leqslant 1$ and $|\bar{B}| \leqslant 1$, we obtain

$$\begin{aligned} \left|P(\hat{a},\hat{b}) - P(\hat{a},\hat{b}')\right| &\leqslant \int \mathrm{d}\lambda \rho(\lambda)\left(1 \pm \bar{A}(\hat{a}',\lambda)\bar{B}(\hat{b}',\lambda)\right) \\ &\quad + \int \mathrm{d}\lambda \rho(\lambda)\left(1 \pm \bar{A}(\hat{a}',\lambda)\bar{B}(\hat{b},\lambda)\right) \\ &= 2 \pm \left(P(\hat{a}',\hat{b}') + P(\hat{a}',\hat{b})\right) \end{aligned}$$

or, more symmetrically,

$$\left|P(\hat{a},\hat{b}) - P(\hat{a},\hat{b}')\right| + \left|P(\hat{a}',\hat{b}') + P(\hat{a}',\hat{b})\right| \leqslant 2.$$

2. Efficiency Loophole

The generation of a pair of photons through SPDC is a stochastic process; it is thus not possible to know beforehand if a pump pulse will generate a pair. Furthermore, the losses in the light path and the non-unitary efficiency of the detectors do not allow for the detection of all the generated photon pairs. It is thus only possible to have outcomes for a restricted sample of all the generation events. In turn, we can only evaluate the correlations over the subspaces (which could be in general dependent on the measurement settings a and b) of the original hidden variable space Λ, which lead to detections at both measurement stations:

$$\Lambda_{D_A D_B}(a,b) \stackrel{\text{def}}{=} \left\{\gamma \in \Lambda \mid \text{det. at } A \cap \text{det. at } B, \text{ for settings } a \text{ and } b\right\}. \tag{A2}$$

As the detection on one side is considered independent of the measurement setting on the other side, we can express these sets as intersections:

$$\begin{aligned} \Lambda_{D_A D_B}(a,b) &= \Lambda_{D_A}(a) \cap \Lambda_{D_B}(b) \\ &\stackrel{\text{def}}{=} \left\{\gamma \in \Lambda \mid \text{det. at } A \text{ for setting } a\right\} \\ &\quad \cap \left\{\gamma \in \Lambda \mid \text{det. at } B \text{ for setting } b\right\}; \end{aligned} \tag{A3}$$

however, the dependence on the local phase settings does not allow to derive the CHSH inequality bound of two for the combination of correlations computed over the restricted hidden variable spaces giving coincidences

$$\begin{aligned} &\left|E_{\Lambda_{D_A D_B}(1,1)}(A_1 B_1) + E_{\Lambda_{D_A D_B}(1,2)}(A_1 B_2)\right| \\ &\quad + \left|E_{\Lambda_{D_A D_B}(2,1)}(A_2 B_1) - E_{\Lambda_{D_A D_B}(2,2)}(A_2 B_2)\right|, \end{aligned} \tag{A4}$$

which are the only ones that we can estimate experimentally. It is indeed not possible to proceed with the original proof, as the sum of expected values over different subspaces cannot be set equal to the expected value of the sum:

$$\begin{aligned} &E_{\Lambda_{D_A D_B}(1,1)}(A_1 B_1) + E_{\Lambda_{D_A D_B}(1,2)}(A_1 B_2) \\ &\quad = \int_{\Lambda_{D_A D_B}(1,1)} A_1(\lambda) B_1(\lambda) \rho(\lambda) \mathrm{d}\lambda \\ &\quad + \int_{\Lambda_{D_A D_B}(1,2)} A_1(\lambda) B_2(\lambda) \rho(\lambda) \mathrm{d}\lambda. \end{aligned} \tag{A5}$$

Any experiment trying to use correlations estimated on these subspaces giving an S parameter greater than two to claim a violation of local realism without additional hypothesis would thus fall into the detection (or efficiency) loophole. It has actually been shown that a Bell inequality can still be derived in this case but the local realistic bound increases with inefficiency so a violation by quantum states is not always possible [62].

3. Fair-Sampling Hypothesis and Post-Selections Independent of Phase Settings

Some kind of fair-sampling hypothesis can nevertheless be used to restore the bound of two on the correlations estimated from coincident detections. If we make the hypothesis that the set of hidden variables leading to joint detections does not depend on the phase settings, $\Lambda_{D_A D_B}(a,b) = \Lambda_{D_A D_B}$, we can indeed proceed as in the original proof and derive a bound for

$$\begin{aligned} &\left|E_{\Lambda_{D_A D_B}}(A_1 B_1) + E_{\Lambda_{D_A D_B}}(A_1 B_2)\right| \\ &\quad + \left|E_{\Lambda_{D_A D_B}}(A_2 B_1) - E_{\Lambda_{D_A D_B}}(A_2 B_2)\right|, \end{aligned} \tag{A6}$$

which would then allow for an experimental violation. We note that less restrictive hypotheses, like assuming that a local realistic model describes the ideal outcomes and that the probabilities of joint detection are independent of the settings, are actually sufficient to restore the bound (see pp. 17 of Ref. [9]).

The first step of our Bell test data analysis consists of only considering the events where two photons have been detected and assuming fair sampling to maintain the validity of the original CHSH inequality.

The second step consists of discarding the cases, deriving from the hug configuration, where the two photons ended up at the same receiver. This subset can be shown to be independent of remote and local phase settings as shown in Ref. [29], so we can indeed maintain the bound of two on $\Lambda_{D_A D_B}$.

The third step of the procedure is particular to the use of the hug interferometer with time-bin sources. It consists of locally discarding detections of photons that did not fall into the central time-bin. In an ideal version of the experiment, we expect the sets of events post-selected by the two partners to be identical and thus independent of phase settings due to the geometry of the hug interferometer, which maintains the time correlation of the pair. This would allow to maintain once more the validity of the CHSH inequality with a bound of two on the set of hidden variables leading to post-selection by both partners $\Lambda_{S_A S_B} = \Lambda_{S_A S_B}(a, b)$, with

$$\Lambda_{S_A S_B}(a, b) \overset{\text{def}}{=} \left\{\gamma \in \Lambda_{D_A D_B} \mid \text{sel. at } A \cap \text{sel. at } B, \text{ for settings } a \text{ and } b\right\}, \tag{A7}$$

by applying the original proof, as we explain in the main text.

Alice and Bob can, independently, post-select the detections in the central time-bin and they will end up with the same set of events. In a Bell test scenario, the measurement settings are randomly switched fast enough to guarantee space-like separation of the measurement choices. In that way, the post-selection at Alice cannot depend on the measurement choice of Bob and vice-versa. The post-selection could still depend on the local measurement settings, but if it did one detection would be selected by Alice and independently discarded by Bob (or vice-versa) for some hidden variables, as the selections would depend on the local measurement setting choices that are assumed to be independent random variables. Thus, obtaining an equal set of post-selected events without communication certifies that the set of post-selected coincidences is independent of the measurement settings. In that case, there is no change of ensemble for the estimation of the correlations in the various measurement settings and the original CHSH inequality can be applied [62].

4. Post-Selection Depending on Local Phase Settings Only

Unfortunately, experimental limitations make this certification impossible, so a different strategy must be adopted as described in the main text.

In practice, it may happen that a detection happens on the central peak for one of the partners and on a lateral peak for the other. This can mainly be caused by double pairs, failed separation of the signal and idler photons, and, finally, detection temporal jitter. Considering this, the independence from local phase settings of the post-selection can no longer be guaranteed; however, the post-selection remains local. The post-selection of events is said to be local if it only depends on the state hidden variable and on the local measurement setting. In that case, the discarded events can be considered as missing detections and approaches developed to close the efficiency loophole can be applied. One of them, proposed in Ref. [63], consists of assigning a fixed outcome of zero to events undetected (in our case, locally discarded) by only one partner. With this approach, the original local-realist CHSH bound of two holds on the union of events where at least one partner detected (in our case, locally post-selected) a photon. These events will lower the violation but thanks to the geometry of the hug configuration they will remain very rare and mainly due to higher order emissions of the generation process.

The CHSH inequality as stated in the first section allows for outcomes to take arbitrary values with the only condition of having their absolute value bounded by one. It is thus possible to assign the outcome of zero when the photons are detected outside the central time-bin. This is proposed in Ref. [63] to deal with the detection loophole; as detection at each receiver is assumed to only depend on the hidden variable and local measurement settings, it can be assimilated to an outcome. Furthermore, a simplification, critical to closing the post-selection loophole, is applicable. The correlations can be estimated by using a redefinition of the correlation computed by omitting the case where the outcome is zero at both receivers. Let

$$\Lambda_{S_A \cup S_B}(a, b) \overset{\text{def}}{=} \left\{\gamma \in \Lambda_{D_A D_B} \mid A \neq 0 \cup B \neq 0, \text{ for settings } a \text{ and } b\right\}. \tag{A8}$$

The authors define in Eq. (1.7) of Ref. [63], using our notation, the correlations

$$e(A_a, B_b) = \frac{\int_{\Lambda_{S_A \cup S_B}(a,b)} A_a(\lambda) B_b(\lambda) \rho(\lambda) \mathrm{d}\lambda}{\int_{\Lambda_{S_A \cup S_B}(a,b)} \rho(\lambda) \mathrm{d}\lambda} \tag{A9}$$

and demonstrate without additional hypothesis that if data are compatible with local realism then the relation in Eq. (1.5) of Ref. [63] must hold:

$$|e(A_1 B_1) + e(A_1 B_2)| + |e(A_2 B_1) - e(A_2 B_2)| \leqslant 2. \tag{A10}$$

We can see that the bound is still that of the original CHSH inequality, so the post-selection procedure proposed and implemented in our paper does not suffer from the post-selection loophole.

APPENDIX B: INDISTINGUISHABILITY CONDITION FOR INTERFERENCE IN THE HUG CONFIGURATION

In this section, we aim to highlight a feature of the hug configuration that was not explicitly mentioned in previous publications [28–32] but might be of interest to the experimentalist. As we will show, the visibility of two-photon interference in the hug configuration depends on the indistinguishability of the two input photons, which is not the case with the Franson interferometer. Of course, this follows from the fact that the interfering processes are the ones where the signal photon goes to Alice and the idler photon goes to Bob and the one where the signal goes to Bob and the idler to Alice. If, in the detection process, some information about which of the two photons is detected on each side can be obtained (even in principle), then, which-path information is obtained at the same time, leading to a reduction of the interference visibility. In our derivation in the main text, we considered identical wavepackets at each input. But what if the two wavepackets have distinguishable temporal profiles despite belonging to the same time-bin?

The wavepacket of the photon in C at time-bin n is rewritten as $c_n^\dagger|0\rangle$ and the wavepacket of the photon in D is rewritten as $\tilde{d}_n^\dagger|0\rangle$, where the tilde will mark the difference between the two input photons. Now, after the full measurement interferometers, the transformation is

$$c_n^\dagger \to \frac{1}{2}\left[e^{i\phi_{A_L}}\left(-a_{+,n+1}^\dagger + ia_{-,n+1}^\dagger\right) + e^{i\phi_{B_S}}\left(b_{+,n}^\dagger + ib_{-,n}^\dagger\right)\right], \tag{B1}$$

$$\tilde{d}_n^\dagger \to \frac{1}{2}\left[e^{i\phi_{B_L}}\left(-\tilde{b}_{+,n+1}^\dagger + i\tilde{b}_{-,n+1}^\dagger\right) + e^{i\phi_{A_S}}\left(\tilde{a}_{+,n}^\dagger + i\tilde{a}_{-,n}^\dagger\right)\right]. \tag{B2}$$

With respect to the previous case, now we have different output modes' creation operators (with and without the tilde), corresponding to slightly distinguishable wavepackets. The input state is now written as

$$|\Phi_{\text{in}}\rangle \triangleq \frac{1}{\sqrt{2}}\left(c_1^\dagger\tilde{d}_1^\dagger + e^{i\phi_p}c_2^\dagger\tilde{d}_2^\dagger\right)|0\rangle \tag{B3}$$

and transformed by the measurement interferometers into

$$\begin{aligned}
&\frac{1}{4\sqrt{2}}\left[e^{i\phi_{A_L}}\left(ia_{-,2}^\dagger - a_{+,2}^\dagger\right) + e^{i\phi_{B_S}}\left(b_{+,1}^\dagger + ib_{-,1}^\dagger\right)\right] \\
&\left[e^{i\phi_{B_L}}\left(i\tilde{b}_{-,2}^\dagger - \tilde{b}_{+,2}^\dagger\right) + e^{i\phi_{A_S}}\left(\tilde{a}_{+,1}^\dagger + i\tilde{a}_{-,1}^\dagger\right)\right]|0\rangle \\
+&\frac{e^{i\phi_p}}{4\sqrt{2}}\left[e^{i\phi_{A_L}}\left(ia_{-,3}^\dagger - a_{+,3}^\dagger\right) + e^{i\phi_{B_S}}\left(b_{+,2}^\dagger + ib_{-,2}^\dagger\right)\right] \\
&\left[e^{i\phi_{B_L}}\left(i\tilde{b}_{-,3}^\dagger - \tilde{b}_{+,3}^\dagger\right) + e^{i\phi_{A_S}}\left(\tilde{a}_{+,2}^\dagger + i\tilde{a}_{-,2}^\dagger\right)\right]|0\rangle.
\end{aligned} \tag{B4}$$

If we focus on the contributions in time-bin 2, where one photon arrives at Alice and one at Bob, then the relevant terms are written as

$$\begin{aligned}
&\frac{e^{i\left(\phi_{A_L}+\phi_{B_L}\right)}}{4\sqrt{2}}\left[\left(a_{+,2}^\dagger - ia_{-,2}^\dagger\right)\left(\tilde{b}_{+,2}^\dagger - i\tilde{b}_{-,2}^\dagger\right)\right. \\
&\left.+\, e^{2i\Delta\phi}\left(\tilde{a}_{+,2}^\dagger + i\tilde{a}_{-,2}^\dagger\right)\left(b_{+,2}^\dagger + ib_{-,2}^\dagger\right)\right]|0\rangle
\end{aligned} \tag{B5}$$

using again $\Delta\phi$ as defined in Eq. (6). The probability of detecting at time-bin 2 a photon in A_μ and one in B_ν with $\mu, \nu \in \{-1, +1\}$ is

$$\begin{aligned}
p_{A_\mu,B_\nu}^{(2,2)}(\Delta\phi) &= \frac{1}{32}\left|\left(a_{\mu,2}^\dagger\tilde{b}_{\nu,2}^\dagger + e^{2i\Delta\phi_{\mu\nu}}\tilde{a}_{\mu,2}^\dagger b_{\nu,2}^\dagger\right)|0\rangle\right|^2 \\
&= \frac{1}{16}\left[1 + |\gamma|^2\cos(2\Delta\phi_{\mu\nu})\right],
\end{aligned} \tag{B6}$$

where $\Delta\phi_{\mu\nu} \triangleq \Delta\phi + \frac{\pi}{4}(\mu - \nu)$ and γ is the overlap between the two inputs modes, namely,

$$\gamma = \langle 0|a_{\mu,2}\tilde{a}_{\mu,2}^\dagger|0\rangle = \langle 0|b_{\nu,2}\tilde{b}_{\nu,2}^\dagger|0\rangle, \tag{B7}$$

whose squared modulus, as shown, represents the interferometric visibility in the central time-bins:

$$V_{A,B}^{(2,2)} = \frac{\frac{1}{16}\left(1 + |\gamma|^2\right) - \frac{1}{16}\left(1 - |\gamma|^2\right)}{\frac{1}{16}\left(1 + |\gamma|^2\right) + \frac{1}{16}\left(1 - |\gamma|^2\right)} = |\gamma|^2. \tag{B8}$$

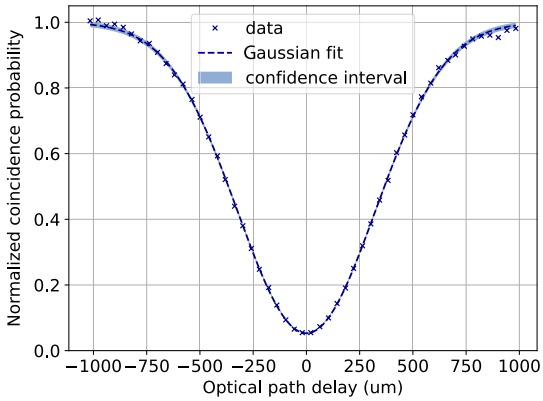

Fig. 8. Hong-Ou-Mandel dip shown as a variation of the coincidence detection probability (normalized to one) with the relative delay between the signal and idler photons impinging on the two inputs of a 50:50 beamsplitter. A coincidence window of 100 ps was used. The area shaded in blue represents a confidence interval of one standard deviation assuming Poissonian counts.

Note that this feature is not a consequence of using a time-bin state as input; the same applies to the energy-time case. This condition on the input state is analogous to the indistinguishability condition required to observe high contrast Hong-Ou-Mandel (HOM) interference [74]. HOM interference can thus be used to characterize the indistinguishability of the two input photons and obtain an upper bound on the two-photon interference visibility obtained with any interferometer in the hug configuration. We tested our SPDC source and obtained a visibility of $94.7 \pm 0.5\%$; the HOM dip is shown in Fig. 8. We believe that spectral differences between the signal and idler in type-II SPDC are responsible for this distinguishability as other degrees of freedom could be finely tuned.

As indistinguishability in all degrees of freedom is required, it is essential to precisely match the arrival time of the signal and idler photons at the input beam-splitters of the hug interferometer. In our setup, the polarization dispersion in polarization-maintaining fibers was sufficient to spoil the interference and we thus had to insert in the setup an optical delay line to compensate for this delay. A scan of the delay to find the position of maximal interference is shown in Fig. 9.

As we have seen, the hug configuration requires the two photons to synchronously enter the input beam-splitters, which is not the case for the Franson interferometer. This can be seen as a disadvantage but there is actually an upside to this feature. Consider the interferometer in the hug configuration of Fig. 1; the path differences between long and short arms for Alice and Bob should be equal in the ideal case [29], that is,

$$l_{A_L} - l_{A_S} = l_{B_L} - l_{B_S}, \tag{B9}$$

where l_X is the optical path-length of path X. Nonetheless, if the manufacturing process is inaccurate and the two differences are not equal it is still possible to obtain the maximal visibility interference in the hug configuration by tuning the delay between signal and idler photons before the interferometer. Let us first consider the energy-time case. As the generation time is unpredictable, the only temporal condition for indistinguishability of the short-short and the long-long processes is to have the difference between the detection time at Alice (t_{A_a}) and the one at Bob (t_{B_b}) to be equal for the two processes. Note that any delay after the output beam-splitters

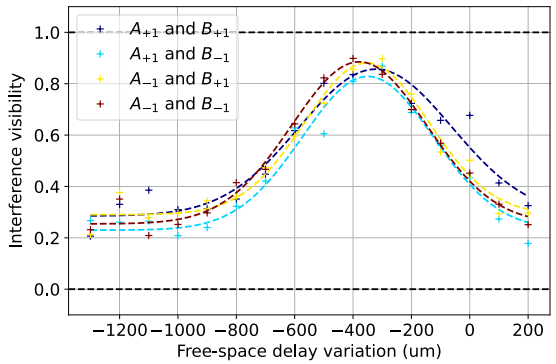

Fig. 9. Scan of the linear stage controlling the delay between signal and idler before the inputs of the interferometer to find the position giving maximal visibility. At each position, measures with different phase settings were taken to have an estimate of the visibility from the variation of the rates of coincidences between the different outputs. Best Gaussian fits are displayed as dashed lines. Note that the estimated visibility does not drop to zero far away from the maximum due to statistical fluctuations in the coincidence counts.

at Alice and Bob is irrelevant, so it can be set to zero without loss of generality. Consider c to be the speed of light in vacuum and an arbitrary generation time t_G for the biphoton; for the short-short case the difference is

$$\tau_{ab}^{SS} = t_{A_a}^{SS} - t_{B_b}^{SS} = \left(t_G + \frac{l_D + l_{A_S}}{c}\right) - \left(t_G + \frac{l_C + l_{B_S}}{c}\right) = \frac{1}{c}\left(l_D + l_{A_S} - l_C - l_{B_S}\right), \tag{B10}$$

while for the long-long case, we have

$$\tau_{ab}^{LL} = t_{A_a}^{LL} - t_{B_b}^{LL} = \left(t_G + \frac{l_C + l_{A_L}}{c}\right) - \left(t_G + \frac{l_D + l_{B_L}}{c}\right) = \frac{1}{c}\left(l_C + l_{A_L} - l_D - l_{B_L}\right). \tag{B11}$$

Therefore, the temporal indistinguishability condition $\tau_{ab}^{SS} = \tau_{ab}^{LL}$ can be rewritten as

$$(l_{A_L} - l_{A_S}) - (l_{B_L} - l_{B_S}) = 2(l_D - l_C). \tag{B12}$$

From this last equation, it is clear that the delay between signal and idler photons before the interferometer can be used to compensate for mismatches in the delays inside the interferometer, which is not possible with a Franson interferometer and could be of particular interest when the interferometer is built with integrated optics. In the time-bin case the possible generation times are known and to have interference we need to verify

$$t_{A_a}^{LL} - t_{A_a}^{SS} = \Delta T = t_{B_b}^{LL} - t_{B_b}^{SS}, \tag{B13}$$

where ΔT is the time difference between the time-bins, which is determined by the delay in the pump interferometer. When Eq. (B12) is satisfied, this leads to

$$\begin{aligned}\Delta T &= t_{A_a}^{LL} - t_{A_a}^{SS} \\ &= \left(t_G + \frac{l_C + l_{A_L}}{c}\right) - \left(t_G + \frac{l_D + l_{A_S}}{c}\right) \\ &= \frac{1}{c}\left(l_C + l_{A_L} - l_D - l_{A_S}\right) \\ &= \frac{1}{c}\left(l_{A_L} - l_{A_S} - \frac{(l_{A_L} - l_{A_S}) - (l_{B_L} - l_{B_S})}{2}\right) \\ &= \frac{(l_{A_L} - l_{A_S}) + (l_{B_L} - l_{B_S})}{2c},\end{aligned} \tag{B14}$$

and thus the compensation is again possible provided the pump interferometer is set to have an imbalance that is the average of the two imbalances in the hug interferometer.

APPENDIX C: SYNCHRONIZATION OF THE TIME-TAGGING SYSTEM WITH THE PUMP LASER RATE FLUCTUATIONS

When using the hug configuration with a time-bin state a local post-selection of the detections in the central time-bin is necessary as detailed in Section 2.B of the main text. If the ratio between the standard deviation of the detection time distribution and the time-bin separation is too low, detections in different time-bins cannot be clearly discriminated. This entails a reduction of the violation of the Bell inequality in two ways. First, we might post-select a pair of photons that actually belonged to the lateral time-bins and thus displays no correlation in the outcomes. Second, we might have cases where one photon is post-selected by one of the parties but not by the other because it was detected outside of its coincidence window. In that case, a fixed outcome (independent of the phase settings) has to be assigned, so the violation is also lowered. Given that the delay line in our PIC was only 2 cm long, corresponding to about $\Delta T = 116$ ps of delay, it was essential for us to optimize the precision of the detection time measurements. In Fig. 10, a simulation of the maximal Bell parameter attainable with local post-selection with respect to the standard deviation of detection times of photons belonging to a given time-bin is displayed.

Our entangled states source was based on the pumping of a SPDC crystal by a mode-locked Ti:sapphire laser (Coherent MIRA) whose repetition rate is 76 MHz. We used Single Quantum Eos SNSPD detectors (whose channels' RMS nominal jitter ranges from 6.0 ps to 9.4 ps) and a Qutools QuTAG time-tagger with jitter upgrade (guaranteeing an RMS jitter lower than 4.5 ps), but this precision would have been useless without properly locking the time-tagger to the fluctuations of the pump laser repetition rate. As the QuTAG can only lock to 10 MHz clock signals, we first electronically derived from the pulse signal at 76 MHz (detected by a fast photo-diode) a 10 MHz signal by exploiting the Clocking Wizard Xilinx IP core implemented on a Xilinx Zynq-7000 System-on-Chip. In that way, the histograms displaying the three peaks could be obtained but the three peaks had still consistent overlaps as fitted Gaussians had RMS widths usually ranging between 30 and 35 ps (for 1 s of capture). These figures being consistently higher than what was expected, we investigated the evolution of the detection time moduli of photons in a single time-bin over short times scales. We found fluctuations in the average of

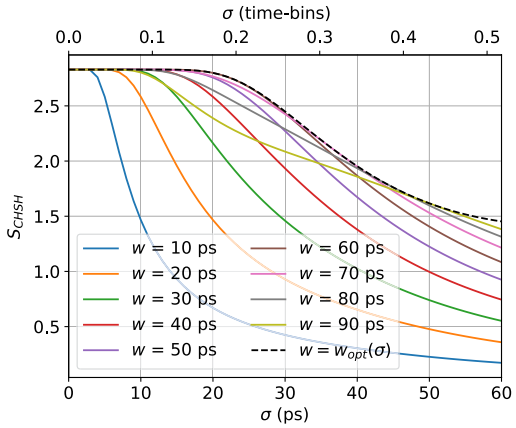

Fig. 10. Theoretical maximum CHSH Bell parameter attainable using an interferometer in the hug configuration in the time-bin case for different local post-selection window half-widths w. S_{CHSH} is plotted against the RMS width σ of detection time distributions of each time-bin (assuming independent Gaussian distributions with means shifted of $\Delta T = 116$ ps). The reduction of the Bell parameter is only due to incorrect discrimination of photons belonging to the different time-bins. Always considering the best window size $w_{\mathrm{opt}}(\sigma)$, we can still see an important drop for $\sigma > 20$ ps, and for $\sigma \geq 40$ ps no violation is possible at all (the classical limit of two is reached for $\frac{\sigma}{\Delta T} \approx 0.335$).

the modulus of the detection time, as displayed in Fig. 11. These fluctuations can probably be explained by convergence delays or residual errors in the synchronization mechanism between the laser and the time-tagger. The fluctuations could span up to tens of picoseconds over a second and had (detectable) frequency components up to the kHz range.

The detection time moduli $d_i(k)$ of photons generated by pulse k that should belong to time-bin $i \in \{1, 2, 3\}$ can thus be modeled as a random process with a fluctuating average $a_i(k) = a_0(k) + i\Delta T$ depending on the accumulated delay between the time-tagger clock and the "laser clock," to which are added several zero-mean random processes: the jitter of the detector j_{det}, the jitter of the time-tagger j_{tag}, and of, finally, the intrinsic uncertainty in the detection time of the photons u_{pho} due to their temporal distribution that we will not explicate but is affected by the pump pulse shape (measured through a field autocorrelator to have an intensity profile with best-fit Gaussian RMS width of 4.35 ± 0.12 ps), by the random generation positions of the biphoton inside the SPDC crystal (which we expect to introduce a variation in the detection time of up to 3.43 ps for a KTP crystal of 20 mm), and by spectral filtering and dispersion effects:

$$d_i(k) = a_0(k) + i\Delta T + u_{\mathrm{pho}} + j_{\mathrm{det}} + j_{\mathrm{tag}}. \tag{C1}$$

The fluctuation of the average $a_0(k)$ is the same for all time-bins, so if it were known it could be removed in post-processing. To estimate $a_0(k)$ we designed a simple algorithm that can be run in real-time. We wanted the estimate to be robust against short-term fluctuations in the distribution of detections among the three time-bins, so the algorithm is composed of a first step to guess which events belong to each time-bin and obtain the estimates for the three $a_i(k)$ and a second step in which the three estimates are combined into an estimate of $a_0(k)$. First, a moving average is computed using the detections in the three time-bins jointly, and it is used to guess with a distance criterion which events belong to the central time-bin and which belong to the lateral ones. Then, for each time-bin we compute again a moving average and interpolate it to all detection times. The differences of the three interpolations of $a_i(k)$ from the expected detection modulus $i\Delta T$ are then combined using a weighted average whose weights are the number of detections used for each interpolation. All tags are then corrected by subtracting this estimate of $a_0(k)$.

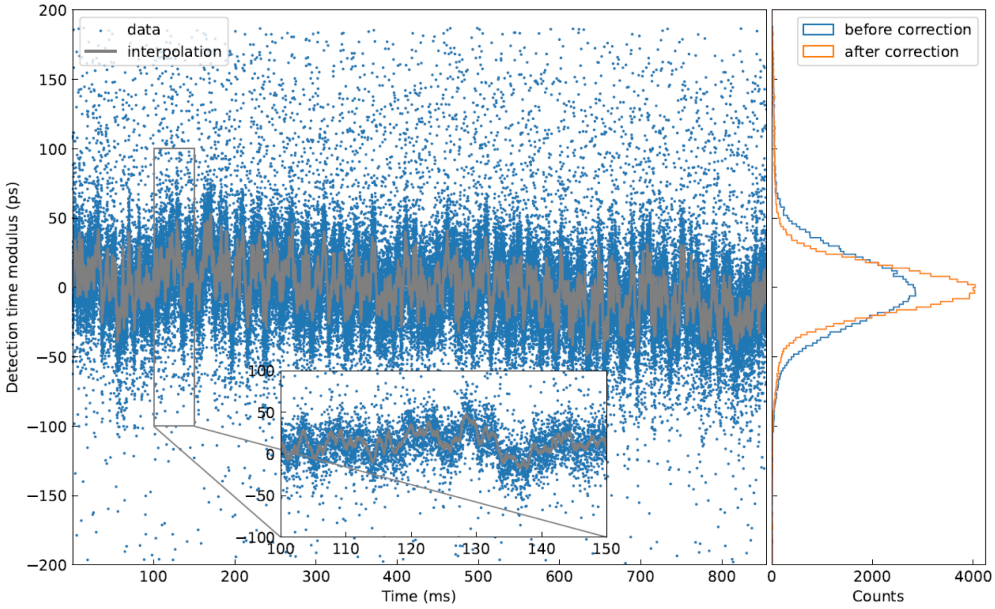

Fig. 11. On the left, a scatter plot of the detection time moduli of photons belonging to time-bin 0 over time is shown. A fluctuation of the average detection time modulus over time due to imperfect locking between the time-tagger and the pump laser is visible. The gray curve displays a cubic interpolation of the moving average (with a window size equal to 50) of the detection time moduli. On the right, the corresponding histograms produced from the raw time-tags and from the time-tags after correction are shown. Note the reduction of the width of the histogram (the best-fit Gaussian RMS width passes from 24.6 ps to 16.8 ps).

Funding. Centrum för Industriell Informationsteknologi, Linköpings Universitet; QuantERA (101017733, 731473); Ministerio de Ciencia, Innovación y Universidades (PCI2019-111885-2); Agencia Estatal de Investigación (PCI2019-111885-2); Ministero dell'Istruzione, dell'Università e della Ricerca ("Departments of Excellence", Law 232/2016); Vetenskapsrådet (VR-2017-0447, VR-2019-0039); Knut och Alice Wallenbergs Stiftelse (Wallenberg Center for Quantum Technology).

Acknowledgment. This work is part of the project SECuRe quantum communication based on Energy-Time entanglement (SECRET), QuantERA Call 2019. We would like to thank Single Quantum for kindly lending us their Eos SNSPDs whose low detection time jitter was essential to achieve the presented results and LioniX for manufacturing the integrated photonics chip.

Disclosures. The authors declare no conflicts of interest.

Data availability. Data underlying the results presented in this paper are not publicly available at this time but may be obtained from the authors upon reasonable request.

REFERENCES

1. R. Horodecki, P. Horodecki, M. Horodecki, *et al.*, "Quantum entanglement," Rev. Mod. Phys. **81**, 865–942 (2009).
2. A. K. Ekert, "Quantum cryptography based on Bell's theorem," Phys. Rev. Lett. **67**, 661–663 (1991).
3. C. H. Bennett, G. Brassard, C. Crépeau, *et al.*, "Teleporting an unknown quantum state via dual classical and Einstein-Podolsky-Rosen channels," Phys. Rev. Lett. **70**, 1895–1899 (1993).
4. M. Hillery, V. Bužek, and A. Berthiaume, "Quantum secret sharing," Phys. Rev. A **59**, 1829–1834 (1999).
5. A. Einstein, B. Podolsky, and N. Rosen, "Can quantum-mechanical description of physical reality be considered complete?" Phys. Rev. **47**, 777–780 (1935).
6. N. Bohr, "Can quantum-mechanical description of physical reality be considered complete?" Phys. Rev. **48**, 696–702 (1935).
7. J. S. Bell, "On the Einstein Podolsky Rosen paradox," Phys. Phys. Fiz. **1**, 195–200 (1964).0554-128X
8. J. F. Clauser, M. A. Horne, A. Shimony, *et al.*, "Proposed experiment to test local hidden-variable theories," Phys. Rev. Lett. **23**, 880–884 (1969).
9. J.-Å. Larsson, "Loopholes in Bell inequality tests of local realism," J. Phys. A **47**, 424003 (2014).
10. B. Hensen, H. Bernien, A. E. Dréau, *et al.*, "Loophole-free Bell inequality violation using electron spins separated by 1.3 kilometres," Nature **526**, 682–686 (2015).
11. M. Giustina, M. A. M. Versteegh, S. Wengerowsky, *et al.*, "Significant-loophole-free test of Bell's theorem with entangled photons," Phys. Rev. Lett. **115**, 250401 (2015).
12. L. K. Shalm, E. Meyer-Scott, B. G. Christensen, *et al.*, "Strong loophole-free test of local realism," Phys. Rev. Lett. **115**, 250402 (2015).
13. W. Rosenfeld, D. Burchardt, R. Garthoff, *et al.*, "Event-ready Bell test using entangled atoms simultaneously closing detection and locality loopholes," Phys. Rev. Lett. **119**, 010402 (2017).
14. M.-H. Li, C. Wu, Y. Zhang, *et al.*, "Test of local realism into the past without detection and locality loopholes," Phys. Rev. Lett. **121**, 080404 (2018).
15. S. Storz, J. Schär, A. Kulikov, *et al.*, "Loophole-free Bell inequality violation with superconducting circuits," Nature **617**, 265–270 (2023).
16. D. P. Nadlinger, P. Drmota, B. C. Nichol, *et al.*, "Experimental quantum key distribution certified by Bell' s theorem," Nature **607**, 682–686 (2022).
17. W. Zhang, T. van Leent, K. Redeker, *et al.*, "A device-independent quantum key distribution system for distant users," Nature **607**, 687–691 (2022).
18. W.-Z. Liu, Y.-Z. Zhang, Y.-Z. Zhen, *et al.*, "Toward a photonic demonstration of device-independent quantum key distribution," Phys. Rev. Lett. **129**, 050502 (2022).
19. S. Pironio, A. Acín, S. Massar, *et al.*, "Random numbers certified by Bell's theorem," Nature **464**, 1021–1024 (2010).
20. Y. Liu, Q. Zhao, M.-H. Li, *et al.*, "Device-independent quantum random-number generation," Nature **562**, 548–551 (2018).
21. L. K. Shalm, Y. Zhang, J. C. Bienfang, *et al.*, "Device-independent randomness expansion with entangled photons," Nat. Phys. **17**, 452–456 (2021).
22. F. Flamini, N. Spagnolo, and F. Sciarrino, "Photonic quantum information processing: a review," Rep. Prog. Phys. **82**, 016001 (2019).
23. J. D. Franson, "Bell inequality for position and time," Phys. Rev. Lett. **62**, 2205–2208 (1989).
24. J. Brendel, N. Gisin, W. Tittel, *et al.*, "Pulsed energy-time entangled twin-photon source for quantum communication," Phys. Rev. Lett. **82**, 2594–2597 (1999).
25. S. Aerts, P. Kwiat, J.-Å. Larsson, *et al.*, "Two-photon Franson-type experiments and local realism," Phys. Rev. Lett. **83**, 2872–2875 (1999).
26. J. Jogenfors and J.-Å. Larsson, "Energy-time entanglement, elements of reality, and local realism," J. Phys. A **47**, 424032 (2014).
27. D. V. Strekalov, T. B. Pittman, A. V. Sergienko, *et al.*, "Postselection-free energy-time entanglement," Phys. Rev. A **54**, R1–R4 (1996).
28. A. Rossi, G. Vallone, F. De Martini, *et al.*, "Generation of time-bin-entangled photons without temporal postselection," Phys. Rev. A **78**, 012345 (2008).
29. A. Cabello, A. Rossi, G. Vallone, *et al.*, "Proposed Bell experiment with genuine energy-time entanglement," Phys. Rev. Lett. **102**, 040401 (2009).
30. G. Lima, G. Vallone, A. Chiuri, *et al.*, "Experimental Bell-inequality violation without the postselection loophole," Phys. Rev. A **81**, 040101 (2010).
31. A. Cuevas, G. Carvacho, G. Saavedra, *et al.*, "Long-distance distribution of genuine energy-time entanglement," Nat. Commun. **4**, 2871 (2013).
32. G. Carvacho, J. Cariñe, G. Saavedra, *et al.*, "Postselection-loophole-free Bell test over an installed optical fiber network," Phys. Rev. Lett. **115**, 030503 (2015).
33. F. Vedovato, C. Agnesi, M. Tomasin, *et al.*, "Postselection-loophole-free Bell violation with genuine time-bin entanglement," Phys. Rev. Lett. **121**, 190401 (2018).
34. J. Jogenfors, A. M. Elhassan, J. Ahrens, *et al.*, "Hacking the Bell test using classical light in energy-time entanglement based quantum key distribution," Sci. Adv. **1**, e1500793 (2015).
35. L. Caspani, C. Xiong, B. J. Eggleton, *et al.*, "Integrated sources of photon quantum states based on nonlinear optics," Light Sci. Appl. **6**, e17100 (2017).
36. G. Moody, L. Chang, T. J. Steiner, *et al.*, "Chip-scale nonlinear photonics for quantum light generation," AVS Quantum Sci. **2**, 041702 (2020).
37. Y. Wang, K. D. Jons, and Z. Sun, "Integrated photon-pair sources with nonlinear optics," Appl. Phys. Rev. **8**, 011314 (2021).
38. H. Jayakumar, A. Predojević, T. Kauten, *et al.*, "Time-bin entangled photons from a quantum dot," Nat. Commun. **5**, 4251 (2014).
39. M. A. M. Versteegh, M. E. Reimer, A. A. van den Berg, *et al.*, "Single pairs of time-bin-entangled photons," Phys. Rev. A **92**, 033802 (2015).
40. M. Prilmüller, T. Huber, M. Müller, *et al.*, "Hyperentanglement of photons emitted by a quantum dot," Phys. Rev. Lett. **121**, 110503 (2018).
41. L. Ginés, C. Pepe, J. Gonzales, *et al.*, "Time-bin entangled photon pairs from quantum dots embedded in a self-aligned cavity," Opt. Express **29**, 4174–4180 (2021).
42. D. Grassani, S. Azzini, M. Liscidini, *et al.*, "Micrometer-scale integrated silicon source of time-energy entangled photons," Optica **2**, 88–94 (2015).
43. R. Wakabayashi, M. Fujiwara, K.-I. Yoshino, *et al.*, "Time-bin entangled photon pair generation from Si micro-ring resonator," Opt. Express **23**, 1103–1113 (2015).
44. C. Reimer, M. Kues, P. Roztocki, *et al.*, "Generation of multiphoton entangled quantum states by means of integrated frequency combs," Science **351**, 1176–1180 (2016).
45. F. Mazeas, M. Traetta, M. Bentivegna, *et al.*, "High-quality photonic entanglement for wavelength-multiplexed quantum communication based on a silicon chip," Opt. Express **24**, 28731–28738 (2016).
46. M. Fujiwara, R. Wakabayashi, M. Sasaki, *et al.*, "Wavelength division multiplexed and double-port pumped time-bin entangled photon pair generation using Si ring resonator," Opt. Express **25**, 3445–3453 (2017).
47. C. Ma, X. Wang, V. Anant, *et al.*, "Silicon photonic entangled photon-pair and heralded single photon generation with CAR>12,000 and $g^{(2)}(0)<0.006$," Opt. Express **25**, 32995–33006 (2017).
48. F. Samara, A. Martin, C. Autebert, *et al.*, "High-rate photon pairs and sequential time-bin entanglement with Si_3N_4 microring resonators," Opt. Express **27**, 19309–19318 (2019).
49. X. Lu, Q. Li, D. A. Westly, *et al.*, "Chip-integrated visible–telecom entangled photon pair source for quantum communication," Nat. Phys. **15**, 373–381 (2019).

50. D. Oser, S. Tanzilli, F. Mazeas, *et al.*, "High-quality photonic entanglement out of a stand-alone silicon chip," npj Quantum Inf. **6**, 31 (2020).
51. T. J. Steiner, J. E. Castro, L. Chang, *et al.*, "Ultrabright entangled-photon-pair generation from an AlGaAs-on-insulator microring resonator," PRX Quantum **2**, 010337 (2021).
52. H. Takesue, Y. Tokura, H. Fukuda, *et al.*, "Entanglement generation using silicon wire waveguide," Appl. Phys. Lett. **91**, 201108 (2007).
53. K.-I. Harada, H. Takesue, H. Fukuda, *et al.*, "Generation of high-purity entangled photon pairs using silicon wire waveguide," Opt. Express **16**, 20368–20373 (2008).
54. H. Takesue, N. Matsuda, E. Kuramochi, *et al.*, "Entangled photons from on-chip slow light," Sci. Rep. **4**, 3913 (2014).
55. P. Sarrafi, E. Y. Zhu, B. M. Holmes, *et al.*, "High-visibility two-photon interference of frequency-time entangled photons generated in a quasi-phase-matched AlGaAs waveguide," Opt. Lett. **39**, 5188–5191 (2014).
56. C. Xiong, X. Zhang, A. Mahendra, *et al.*, "Compact and reconfigurable silicon nitride time-bin entanglement circuit," Optica **2**, 724–727 (2015).
57. C. Autebert, N. Bruno, A. Martin, *et al.*, "Integrated algaas source of highly indistinguishable and energy-time entangled photons," Optica **3**, 143–146 (2016).
58. Y.-H. Li, Z.-Y. Zhou, L.-T. Feng, *et al.*, "On-chip multiplexed multiple entanglement sources in a single silicon nanowire," Phys. Rev. Appl. **7**, 064005 (2017).
59. X. Zhang, B. A. Bell, A. Mahendra, *et al.*, "Integrated silicon nitride time-bin entanglement circuits," Opt. Lett. **43**, 3469–3472 (2018).
60. J. Zhao, C. Ma, M. Rüsing, *et al.*, "High quality entangled photon pair generation in periodically poled thin-film lithium niobate waveguides," Phys. Rev. Lett. **124**, 163603 (2020).
61. C. G. H. Roeloffzen, M. Hoekman, E. J. Klein, *et al.*, "Low-loss Si_3N_4 TriPleX optical waveguides: technology and applications overview," IEEE J. Sel. Top. Quantum Electron. **24**, 4400321 (2018).
62. J.-Å. Larsson, "Bell's inequality and detector inefficiency," Phys. Rev. A **57**, 3304–3308 (1998).
63. A. Garg and N. D. Mermin, "Detector inefficiencies in the Einstein-Podolsky-Rosen experiment," Phys. Rev. D **35**, 3831–3835 (1987).
64. N. Gisin, G. Ribordy, W. Tittel, *et al.*, "Quantum cryptography," Rev. Mod. Phys. **74**, 145–195 (2002).
65. Y. Liu, A. Wichman, B. Isaac, *et al.*, "Tuning optimization of ring resonator delays for integrated optical beam forming networks," J. Lightwave Technol. **35**, 4954–4960 (2017).
66. Y. Liu, A. R. Wichman, B. Isaac, *et al.*, "Ultra-low-loss silicon nitride optical beamforming network for wideband wireless applications," IEEE J. Sel. Top. Quantum Electron. **24**, 8300410 (2018).
67. D. Pérez, J. Fernández, R. Baños, *et al.*, "Thermal tuners on a silicon nitride platform," arXiv, arXiv:1604.02958 (2016).
68. X.-S. Ma, S. Zotter, N. Tetik, *et al.*, "A high-speed tunable beam splitter for feed-forward photonic quantum information processing," Opt. Express **19**, 22723–22730 (2011).
69. X. Zhu, G. Li, X. Wang, *et al.*, "Low-loss fiber-to-chip edge coupler for silicon nitride integrated circuits," Opt. Express **31**, 10525–10532 (2023).
70. S. Al-Obaidi, "Minimizing coupling losses with silicon nitride waveguide tapers," 2023, https://www.lionix-international.com/about-us/blog/minimizing-coupling-losses/.
71. C. Han, Z. Zheng, H. Shu, *et al.*, "Slow-light silicon modulator with 110-ghz bandwidth," Sci. Adv. **9**, eadi5339 (2023).
72. Y. Zhang, J. Nauriyal, M. Song, *et al.*, "Engineered second-order nonlinearity in silicon nitride," Opt. Mater. Express **13**, 237–246 (2023).
73. J. S. Bell, "Introduction to the hidden-variable question," in *John S. Bell on the Foundations of Quantum Mechanics* (1971), pp. 22–32.
74. Z.-Y. J. Ou, *Multi-Photon Quantum Interference* (Springer, 2007).